Sensors and Materials, Vol. 38, No. 5 (2026) 2871–2890
MYU Tokyo

S & M 4475

Sensor-Integrated Heat Dissipation Design and Its Optimization for Routers with Thermal Load

Min-Chie Chiu,[1*] Ho-Chih Cheng,[2] Yu-HsinWang,[1]
Shih-Ming Cho,[3] and Tian-Syung Lan[4]

[1]Department of Mechanical and Materials Engineering, Tatung University,
No. 40, Sec. 3, Zhongshan N. Rd., Taipei City 10452, Taiwan
[2]Department of Intelligent Manufacturing Technology, Ling Tung University,
No. 1, Ling Tung Rd., Taichung City 40852, Taiwan
[3]Department of Computer Science and Engineering, Tatung University,
No. 40, Sec. 3, Zhongshan N. Rd., Taipei City 10452, Taiwan
[4]Department of Information Management, Yu Da University of Science and Technology,
Miaoli County 361, Zaoqiao Township, Taiwan

(Received March 31, 2026; accepted May 8, 2026)

Keywords: temperature sensors, thermal monitoring, CFD, cooling, controller, router system, optimization, control

In the era of 5G and big data transmission, heat dissipation challenges for critical components such as CPUs and bi-directional optical sub-assembly (BOSA) modules must be addressed. In this study, we developed an intelligent, sensor-integrated cooling design that combines high thermal conductivity materials with topology-based flow field optimization to enhance thermal reliability. A hybrid structure of natural and forced convection was employed, regulated by embedded temperature sensors and a microcontroller. When component temperatures approached their operational limits (90 °C for BOSA and 105 °C for CPU), the system activated a 6.0 mm fan to ensure safe operation. Experimental validation tests and high-fidelity computational fluid dynamics simulations were conducted using calibrated K-type thermocouples and the SIMPLEST algorithm, respectively. The mesh-independent simulation results confirmed numerical accuracy, with only 0.7% error relative to experimental data. Topology optimization was performed to identify the optimal CPU heat sink parameters (fin height = 20 mm, fin width = 1 mm, and number of fins = 9), reducing CPU temperature to 93 °C. The novelty of this study lies not only in extending prior research on laptop thermal management (primarily focused on CPU-only systems), but also in further applying the control strategy to the thermal design of high-heat-generation routers that incorporate both CPUs and bi-directional optical sub-assembly (BOSA) modules in practical applications. The results demonstrate that shifting sensors from passive monitoring to active regulation significantly improves cooling efficiency, offering a robust framework for next-generation portable electronics under high thermal stress. Future research may further advance this approach by developing optimal fan cooling strategies that dynamically adjust fan speed in response to real-time temperature variations. In addition, given the impact of fan noise on user comfort, subsequent studies should

*Corresponding author: e-mail: mcchiu@gm.ttu.edu.tw
https://doi.org/10.18494/SAM6363

ISSN 0914-4935 © MYU K.K.
https://myukk.org/

integrate acoustic modeling with thermal performance simulations to achieve a balanced design that simultaneously satisfies both noise constraints and cooling efficiency.

1. Introduction

With the continuous miniaturization and performance enhancement of laptop computers, components such as CPUs, routers, and graphics processors are required to operate at higher power densities and frequencies. These advancements inevitably generate substantial localized thermal loads within compact enclosures.(1,2) If not effectively managed, excessive heat dissipation leads to thermal throttling, reduced computational throughput, instability in wireless communication modules, and the accelerated degradation of semiconductor materials.(3,4) This makes robust thermal management strategies indispensable for ensuring the operational reliability and longevity of modern portable computing devices.

Traditional thermal management approaches for small-scale electronics have mainly relied on material innovations. While metals such as copper and aluminum remain widely used for passive cooling solutions, the potential of graphene for heat dissipation in thermal interfaces and heat sinks has been given considerable attention, owing to its thermal conductivity of up to 5000 W/mK.(5)Aluminum nitride, with its high thermal conductivity (170–200 W/mK), also outperforms conventional aluminum oxide in providing electrical insulation and efficient heat transfer.(6) However, since routers continue to demand higher computational throughput, passive material-based solutions alone are insufficient to address rapidly fluctuating thermal loads.(7,8) Effective heat transfer and topology optimization can improve the passive dissipation of the components in small devices, but these methods remain limited in handling dynamic thermal variations inherent in portable computing environments.(9)

To achieve efficient thermal regulation in laptops, the optimization of heat sink topology, airflow pathways, and fan-assisted cooling is essential. Structural designs incorporating multi-channel and branch-optimized geometries have been proven to enhance cooling uniformity and efficiency,(10,11) but such designs require active control mechanisms to adapt to real-time operating conditions. This is where sensor technology plays a transformative role.

The integration of embedded temperature sensors enables intelligent, adaptive heat dissipation strategies. Recent developments in sensor-driven thermal management systems combine real-time monitoring with AI-based predictive analytics, allowing proactive interventions to prevent overheating and extend component lifespan.(12,13) By strategically placing sensors near critical components such as CPUs and routers, continuous feedback can be given to dynamically regulate fan speed, airflow direction, and even operating voltage and frequency.(14,15) Such sensor-guided heal management ensures that cooling mechanisms respond effectively to workload variations and ambient changes, thereby maintaining system stability and performance efficiency.(16) Moreover, sensor integration facilitates hybrid cooling systems that combine natural and forced convection, optimizing both energy efficiency and thermal reliability.(17)

In this study, we present a sensor-integrated thermal management design tailored for routers under high thermal loads. Real-time sensor feedback was used to optimize heat sink topology,

fan behavior, and airflow distribution. The novelty of this study lies not only in extending the prior work of Chen *et al.*[18] on sensor-based thermal monitoring and fan control for laptop cooling (focused on CPU-only systems), but also in further applying the control strategy to the thermal design of high-heat-generation routers incorporating both CPUs and bi-directional optical sub-assembly (BOSA) modules in practical applications. This work establishes an optimized fan control methodology applicable to routers, which are high-power-density electronic communication systems. Compared with most previous studies, which primarily focus on individual components or theoretical analyses, the innovation of this research resides in the integrated framework of "sensor feedback + fan control strategy + system-level thermal design." A hybrid cooling mechanism combining natural and forced convection is employed. By embedding temperature sensors and coupling them with microcontroller-based regulators, we established a responsive cooling strategy to maintain thermal stability under normal operating conditions. Through real-time temperature feedback from embedded thermal sensors and logical decision-making by the controller, fan operation is dynamically regulated to maintain system temperatures within a safe operating range. This approach also represents an energy-efficient thermal management strategy for router applications. The results of this study underscore the importance of sensor technology in advancing intelligent thermal management for compact computing devices, contributing to improving device reliability and the development of sensor applications in next-generation portable electronics.

2. Methodology

2.1 Experimental setup

To validate the sensor-integrated heat dissipation design, an experimental platform was constructed to monitor the thermal behavior of the components, involving network communication under controlled conditions. Temperature data were acquired using calibrated K-type thermocouples positioned at critical thermal junctions, including a CPU and the bi-directional optical sub-assembly (BOSA) modules. The sensor placement is shown in Fig. 1, ensuring the high-fidelity monitoring of the components most susceptible to thermal load. K-type thermocouples were adhered to the following three heat-generating sources: the CPU, the BOSA module, and the 10G controller. These sensors provide the high-fidelity transient temperature data required to validate the numerical simulations. The wiring was carefully routed to minimize interference with the internal airflow vectors generated by the 6.0 mm cooling fan. The specification of sensors is presented in Table 1.

To replicate extreme operational scenarios, the entire assembly was placed within a thermal-controlled chamber. The ambient temperature of the testing environment was maintained at a constant 60 ℃ (Fig. 2). This setup was used to simulate the internal thermal stress, which is typical of router enclosures during high-intensity processing. The data obtained from this setup was used as the baseline for verifying the accuracy of the subsequent numerical simulations.

To facilitate the forced convection required for high thermal load scenarios, a high-performance, ultraslim cooling fan was integrated into the router assembly. The fan measures 87

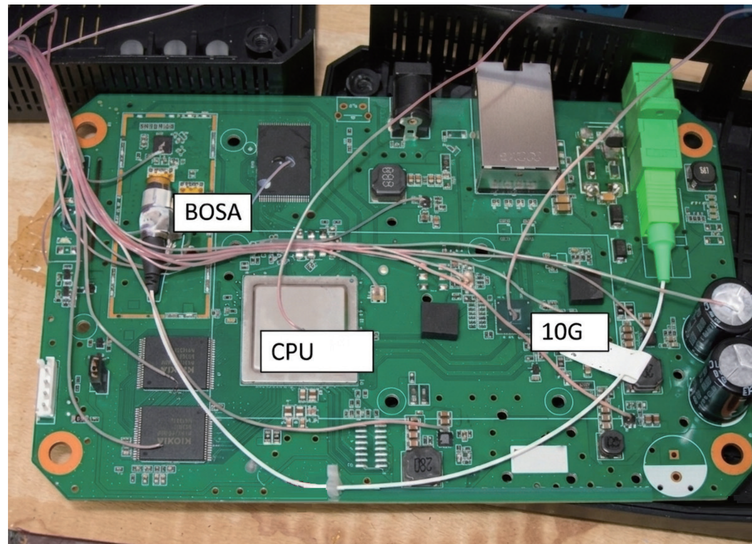

Fig. 1. (Color online) Experimental setup for thermal measurement: thermocouple placement on network communication and CPU modules (10G: 10 Gigabit Ethernet (10GbE) controller).

Table 1
Specifications of thermal sensors used in the intelligent cooling system.

Feature	Description
Sensor type	K-type Thermocouples & Integrated Thermal Diodes
Placement	CPU Junction, BOSA Module, Chassis Air Intake
Sampling rate	Real-time monitoring via microcontroller
Function	Trigger for 3-phase fan actuator (forced convection)
Purpose	Prevention of thermal throttling and breach of component specs

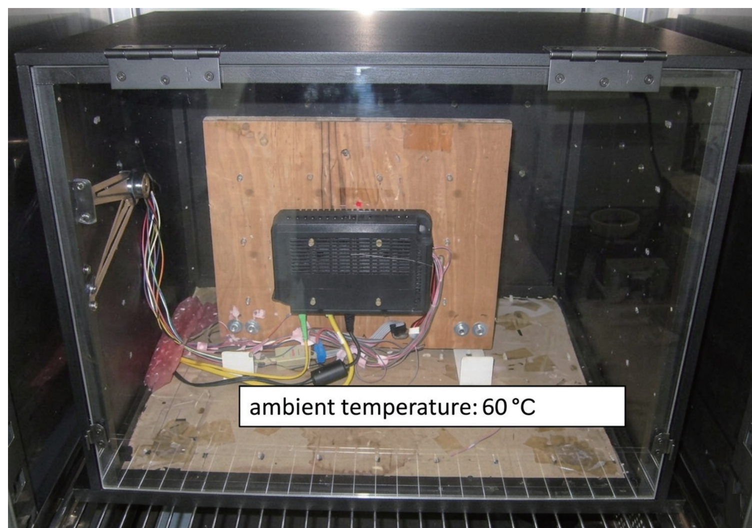

Fig. 2. (Color online) Experimental setup for thermal measurement: thermocouple placement on network communication and CPU modules (10G: 10 Gigabit Ethernet (10GbE) controller).

× 85 × 6.0 mm^3, specifically selected to fit the compact 3D stacking architecture of the device without increasing its overall footprint. The fan's mechanical design is optimized for durability and acoustic efficiency. It features a 3-phase brushless motor and a fluid dynamic bearing with a copper bushing, ensuring stable operation during long-duration thermal stress tests. The fan blades, with a thickness of only 0.15 mm, are manufactured from a liquid crystal polymer to prevent material deformation at high rotational speeds. Additionally, the fan housing incorporates 5% ocean bound plastic, aligning the hardware specifications with sustainable manufacturing practices. In the experiment, this fan serves as the system's actuator. It remains inactive during standard operations to allow for natural convection but is dynamically triggered by the microcontroller once the embedded sensors detect that the CPU or BOSA temperatures have reached their respective manufacturer specifications (Tables 2–4).

Table 2
Selected parameters for high-temperature design.

Parameter	Without fan	With fan
Temperature	60–80 °C	60–90 °C
CPU power (W)	5.6	5.6
Maximum operating temperature of CPU/BOSA	105/90 °C	105/90 °C

Table 3
Heat module specifications (electrical control part specifications).

Component	Thermal module design
Fan	87 × 85 × 6.0 mm^3 (length × width × height) Blade thickness 0.15 mm (liquid crystal polymer)/fluid dynamic bearing, Cu bushing NdFeB magnets, 3-phase motor Pillow (thickness of 0.5 mm, steel use stainless 304) Cover (thickness of 0.4 mm, steel use stainless 304) Fan housing (5% of ocean bound plastic)
Grease	Thermal conductivity K = 5 (W/m·k)
Heat sink	Aluminum 6063 with anodizing
Thermal design power	CPU 5.6 W 10G 2.4 W

Table 4
Specifications of fan for forced convection.

Power supply	DC
Direction of fan rotation	Counter clockwise
Rated voltage	5.0V
Minimum start voltage or duty	20% at 5 V
Safety certification current	0.5A
Maximum power at 4000 revolutions per minute (RPM)	2.5W4000 RPM
Fan speed at 5 V	4000 ± 7%
Fan speed at start	1350 ± 200
Maximum air pressure at start	12.8 Pa (minimum of 11.9)
Flow rate with zero air	5.5 ft^3
Sound pressure level	38 (maximum 45) dB
Insulation resistance	10 MΩ at DC 500 V

2.2. Heat sink design

The heat sink topology for BOSA and CPU was designed as a critical passive dissipation layer. The design includes parameters for the number, height, and width of cooling fins, which are optimized to capture and redistribute localized thermal loads. Table 5 presents the geometric variables used in the design of heat sinks and ventilation apertures.

The gap between heat sinks (F_g) and the total length of the heat sink module (F_{tt}) is crucial for determining the airflow resistance. This resistance is an important factor for temperature sensors to monitor and determine when active cooling (the fan) is required (Figs. 3 and 4). The ventilation apertures in the device's molded plastic chassis were positioned to facilitate natural and forced convection. The casing hole was centered on the aperture. The widths of the inlet (H_d) and upper inlet (H_{d2}) affect the air volume and airflow velocity at the entrance. For instance, adjusting H_d to 3 mm and H_{d2} to 5mm significantly reduced CPU temperature by improving the exhaust efficiency. When the sensors detect temperatures approaching the tolerable limits, 90 °C for BOSA and 105 °C for CPU, the controller activates the fan to enhance cooling beyond what the passive heat sink and vent design can provide.

Table 5
Design variables for heat dissipation.

Component	Variable	Description
Exhaust vent	H_d	Width of main outlet vent
	H_{d2}	Width of upper outlet vent
CPU heat sink	F_h	Height of CPU cooling fins
	F_w	Width of CPU cooling fins
	F_n	Number of CPU cooling fins
BOSA heat sink	F_{h1}	Height of BOSA cooling fins
	F_{w1}	Width of BOSA cooling fins
	F_{n1}	Number of BOSA cooling fins
Module parameters	F_g/F_{g1}	Spacing between cooling fins (CPU/BOSA)
	F_{TT}/F_{TT1}	Total length of heat sink module (CPU/BOSA)

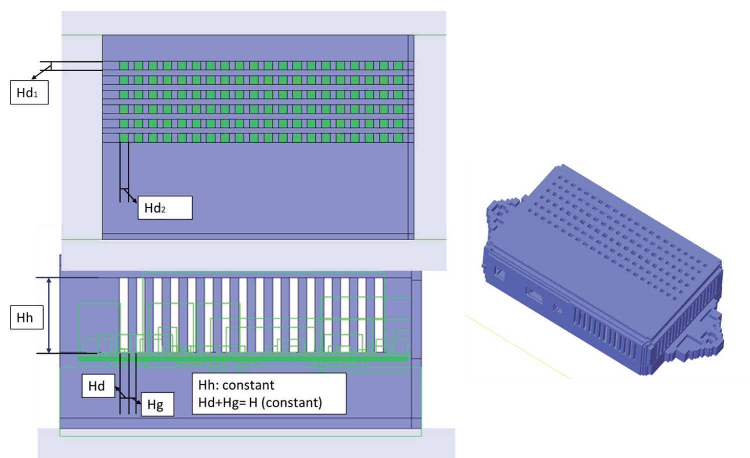

Fig. 3. (Color online) Design of heat exhaust vents for relevant network communication products.

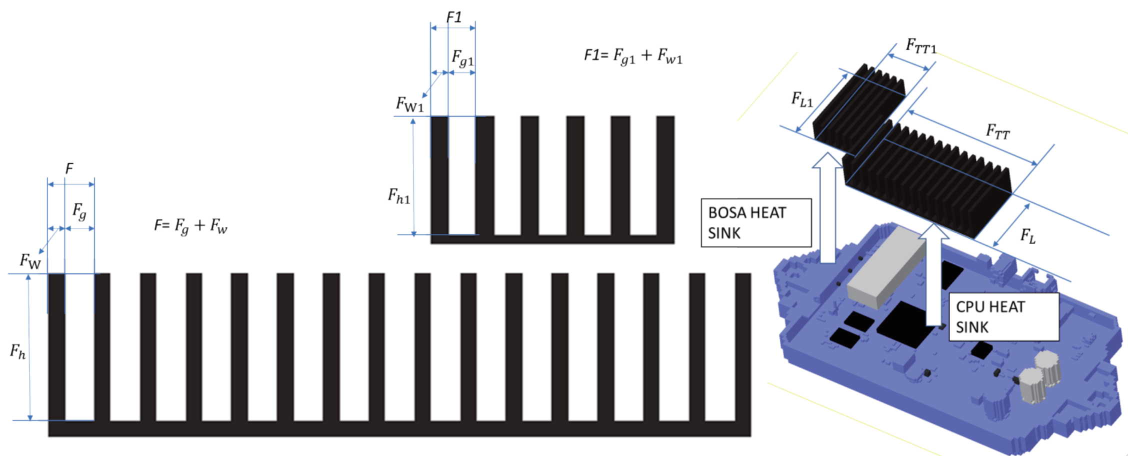

Fig. 4. (Color online) Design of heat sinks for relevant network communication products.

2.3 Model design for simulation

To evaluate the thermal performance of the laptop system, a high-fidelity numerical model was developed in this study. A physical 3D geometry created by computer-aided design was used to construct a computational fluid dynamics (CFD) model, ensuring that simulated thermal gradients closely align with experimental measurements. The 3D stacking structure of the router is illustrated in Fig. 5.

The device features a compact size of 169 × 50 × 29.9 mm^3 and is lightweight (about 500 g). The chassis is composed of molded plastic with strategically positioned ventilation apertures to facilitate heat dissipation. The internal stacking architecture of the router is a compact integration of high-heat-generating components and their respective thermal management interfaces. The design accounts for the vertical orientation of the device, as indicated by the gravity direction, which affects natural convection patterns within the enclosure. Internal elements included the following.

- Primary heat sources (BOSA and CPU): BOSA and CPU are the dominant heat generators, mounted directly onto the router mainboard.
- Thermal interface materials (grease): Grease minimizes contact resistance. A layer of thermal grease is applied between CPU and its heat sink, ensuring an efficient conductive pathway.
- Passive dissipation components (heat sinks): BOSA and CPU heat sinks are stacked above the components. Their volume and surface area are optimized to capture and redistribute localized thermal loads.
- Airflow and clearance (gap): Gaps are maintained at the top and bottom of the module. These gaps, combined with the intake (blue arrows) and exhaust (red arrows) ports, facilitate the flow of air across the finned surfaces.
- Peripheral components: Small electrical components are distributed on the board, contributing to the baseline thermal profile of the system.

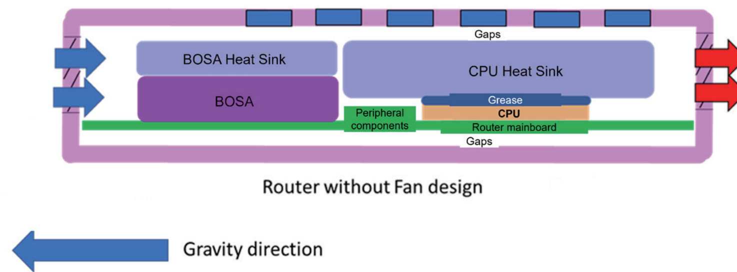

Fig. 5. (Color online) 3D stacking structure of network communication module (excluding fan design).

By modeling the module, the CFD simulation was conducted to predict the steady-state temperature distribution. In the simulation, a hybrid cooling strategy was adopted, including passive cooling (conductive heat transfer through optimized heat sinks) and forced convection (a precision-engineered, low-noise fan assembly expelling accumulated thermal energy). The CFD simulation was conducted for solid-state thermal interfaces and internal airflow dynamics, enabling an accurate representation of combined cooling effects within the confined laptop environment. The accuracy of CFD simulations is affected by grid density. Therefore, to ensure numerical reliability, a mesh independence study was conducted using three configurations (Fig. 6).

- Case A (low density): up to 150000-element mesh
- Case B (medium density): up to 300000-element mesh
- Case C (high density): up to 1000000-element mesh

The simulations were performed by employing the standard k–ϵ turbulence model to capture convective heat transfer coefficients within the compact enclosure. Evaluation through simulations was employed for the identification of the optimal mesh density, balancing computational efficiency with accuracy in predicting thermal gradients.

The temperature gradients were analyzed relative to experimental benchmarks (Table 6). The data summarized in Table 6 were obtained by cross-referencing the results of the steady-state CFD simulations against the empirical measurements obtained in the controlled thermal environment described in this article. While the low-density mesh provided a rapid computational turnaround, the high-density mesh yielded the highest convergence accuracy, with the simulated CPU temperature (102.5 ℃) closely matching the measured value (101.8 ℃). Consequently, the high-density mesh was selected for all subsequent optimization phases.

2.4 Mathematical background

2.4.1 Theoretical equations

The thermal behavior of the system was modeled in FLOTHERM using the finite-volume method, which solves the governing conservation equations of mass, momentum, and energy for electronic cooling applications. In this study, the heat transfer process is represented through the combined effects of conduction, convection, and radiation. Heat conduction in solid materials is governed by Fourier's law, while convective heat transfer between solid surfaces and airflow

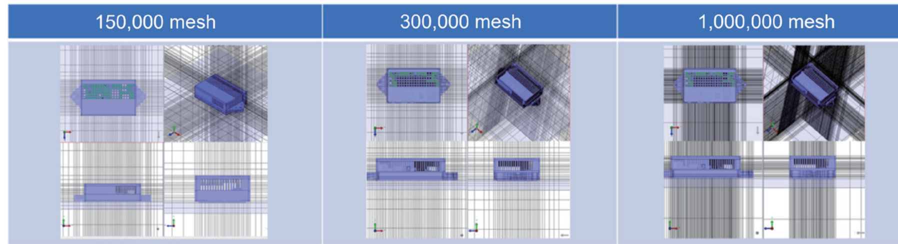

Fig. 6. (Color online) Mesh configuration of network communication module.

Table 6
Simulated and experimental temperatures across mesh densities.

Mesh count	BOSA temperature (°C)	CPU temperature (°C)	Error (relative to CPU data)
150000	78.5	107	5.10%
300000	80.2	105	3.10%
1000000	85.8	102.5	0.70%
Experiment	84.2	101.8	—

follows Newton's law of cooling. Radiative heat exchange is also considered using the Stefan–Boltzmann law, which becomes significant at elevated component temperatures. The overall energy balance in the system can be expressed as

$$Qtotal = Qcond + Qconv + Qrad\,, \tag{1}$$

where each term represents conduction, convection, or radiation heat transfer contribution, respectively.

2.4.2 CFD framework

The airflow within the compact enclosure is treated as a steady-state, incompressible, viscous flow. The solver resolves the following conservation equations.

2.4.2.1 Continuity equation to ensure mass conservation within each control volume

$$\frac{\delta u}{\delta x} + \frac{\delta v}{\delta y} + \frac{\delta w}{\delta z} = 0 \tag{2}$$

Here, u, v, and w are the velocity components in the x-, y-, and z-directions (m/s), respectively. This equation shows that mass is conserved: the amount of air entering a control volume equals the amount of air leaving while accounting for pressure gradients and viscous shear. To simulate natural convection during low-fan-speed states, the Boussinesq approximation is applied in the gravity direction to model buoyancy-driven flow.

2.4.2.2 Momentum equation (Navier–Stokes) to resolve the velocity field

$$\rho\left(\boldsymbol{u}\cdot\nabla\right)\boldsymbol{u} = -\nabla P + \mu\nabla^2\boldsymbol{u} + \rho\boldsymbol{g}\beta\left(T - T_{ref}\right) \tag{3}$$

Here, ρ is the fluid density (kg/m^3), $\boldsymbol{u}$ is the velocity vector (m/s), ∇P is the pressure gradient (Pa/m), μ is the dynamic viscosity (Pa·s), representing internal fluid friction, $\nabla^2 \boldsymbol{u}$ is the viscous diffusion term, $\boldsymbol{g}$ is the gravitational acceleration vector (m/s^2), β is the thermal expansion coefficient (1/K), and $(T - T_{ref})$ is the temperature difference driving buoyancy. Equation (3) models airflow, including buoyancy effects when hot air rises inside the router enclosure.

2.4.2.3 Energy equation to couple fluid dynamics to the temperature field, accounting for heat advection by airflow and conduction through solid interfaces

$$\rho c_p \left(\frac{\partial T}{\partial t} + \boldsymbol{u} \cdot \nabla T \right) = \nabla \cdot \left(k \nabla T \right) + \Phi \tag{4}$$

Here, ρ is the fluid density (kg/m^3), c_p is the specific heat capacity at constant pressure (J/kg·K), T is the temperature (K or °C), $\partial T / \partial t$ is the time rate of change in temperature (for steady-state, this is zero), $\boldsymbol{u} \cdot \nabla T$ is the convective (advective) transport of heat by airflow, k is the thermal conductivity (W/m·K), $\nabla \cdot (k \nabla T)$ is the teat conduction term, describing the diffusion of heat through solids and fluids, and Φ is the viscous dissipation term (W/m^3), representing the conversion of mechanical energy into heat due to fluid friction. In electronics cooling problems, this term is small and often neglected.

2.4.3 Semi-implicit Method for Pressure-linked Equation (SIMPLE)

A challenge in CFD is the coupling of pressure and velocity fields. In this study, the SIMPLEST algorithm was selected because it offers enhanced stability and convergence for complex geometries. SIMPLE uses a guess-and-correct cycle for pressure but often converges slowly in complex 3D geometries. SIMPLE revised (SIMPLER) improves convergence by solving a dedicated pressure equation, reducing the number of iterations, whereas SIMPLE Stability (SIMPLEST) further refines the process by incorporating skew transport terms and improved discretization schemes. SIMPLEST provides complete boundary condition handling and enhanced stability for turbulent flows. In this study, SIMPLEST was used because of the geometric complexity of the router (Fig. 7), where high-density heat sinks and forced convection require numerically stable coupling to ensure energy balance.

The iterative process follows the workflow shown in Fig. 7. To ensure the physical validity of the results, the following constraints were applied.

- Contact resistance: Thermal interface resistances between CPU and the heat sink (thermal grease) were modeled as discrete thin-film layers.
- Convergence criteria: Iterations were continued until the residuals for mass and momentum dropped below 10^{-4} and the energy residual was less than 10^{-7}.
- Gravity alignment: The y-direction was aligned with the negative gravity vector to accurately capture the stack effect of heated air within the enclosure.

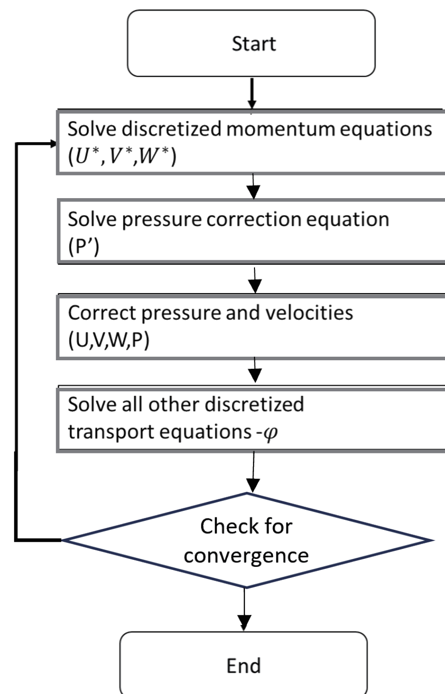

Fig. 7. Computational process for flow and temperature fields in heat dissipation of laptopcomputer components.

3. Results

3.1 Natural convection optimization results

At an ambient temperature of 60 °C, the natural convection optimization for the network device (router) was conducted. Six design parameters [fin height (F_h), fin width (F_w), and the number of fins (F_n) for the CPU heat sink, and F_{h1}, F_{w1}, and F_{n1} for the BOSA heat sink] were selected and combined in a calculation loop (Fig. 8). This resulted in 756 design variations. The process illustrates how the transition from a standard router to a high-performance, sensor-enabled device was achieved through iterative refinement and validation. In the initial CFD simulations, thermal bottlenecks were observed in the 3D stacking structure (Fig. 1), particularly at CPU and 10G components. These hotspots highlighted the limitations of purely material-based cooling solutions. Topology optimization was applied to heat sink geometries to maximize airflow efficiency. The SIMPLEST algorithm was used to predict how micro-changes in fin spacing and arrangement would affect the pressure field and convective heat transfer. For numerical validation, the optimized designs were subjected to mesh independence testing (Fig. 6).

Convergence at the 1000000-element mesh was selected to confirm that the model was sufficiently accurate to simulate extreme environments at 60 and 70 °C. This workflow demonstrates that maximum cooling performance is achieved through improved materials and geometry and the optimized physical architecture. The device maintains structural integrity and operational stability under demanding thermal loads.

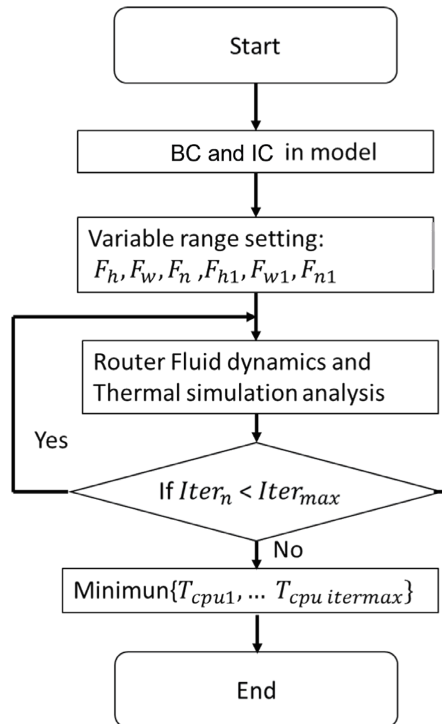

Fig. 8. Engineering optimization process for heat dissipation of components (BC: boundary condition; IC: Initial condition).

The iteration results for CPU and BOSA temperatures are shown in Figs. 9 and 10, while the parameter-specific iterations are presented in Fig. 11. The optimization results indicate that the CPU temperature reached its minimum value of 93 ℃ at the 742nd iteration. The optimal parameters were determined as F_h = 20 mm, F_w = 1 mm, and F_n = 9 for the CPU heat sink, and F_{h1} = 13.6 mm, F_{w1} = 1 mm, and F_{n1} = 2 for the BOSA heat sink. These results confirm that fin geometry strongly affects thermal dissipation: narrower fins and optimized fin numbers improve cooling efficiency, whereas excessive fin density restricts airflow and increases CPU temperature.

Figures 9–11 present converged solutions, where sensor data and structural design intersect to validate the effectiveness of the proposed cooling strategy. The variations in thermal-related parameters under different design factors across multiple configuration settings are shown in Fig. 11. As indicated in Fig. 11, the trends of each parameter under different combinations can be observed, which further facilitates the identification of optimal solutions. These results enable a comparative evaluation of performance differences among various configurations and serve as an important basis for subsequent thermal design optimization and system configuration decisions. The results validate the convergence of numerical modeling. As indicated in Fig. 6 and Table 6, the steady-state temperature distribution of the router under a 60 ℃ ambient condition. It highlights critical monitoring nodes near the CPU and BOSA modules, confirming the necessity of embedding sensors in these locations. Without sensor-triggered forced convection, these zones approach the thermal throttling limit of 101.8 ℃.

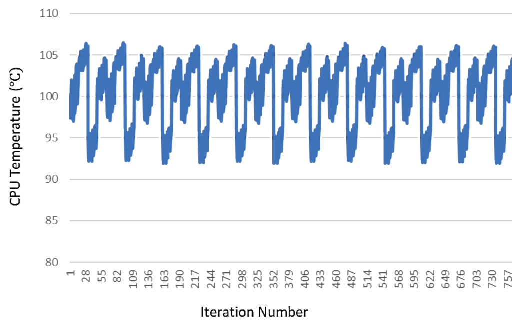

Fig. 9. (Color online) CPU temperature and iteration chart of 756 iterations from the engineering optimization with 1 million grid results.

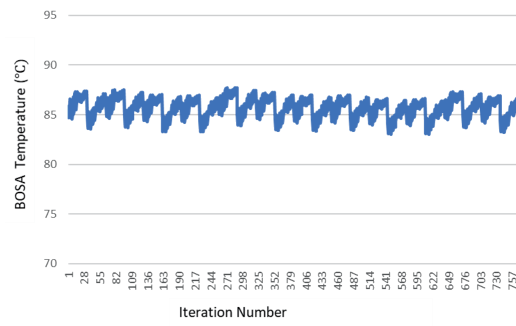

Fig. 10. (Color online) BOSA temperature and iteration chart of 756 iterations from the engineering optimization with 1 million grid results.

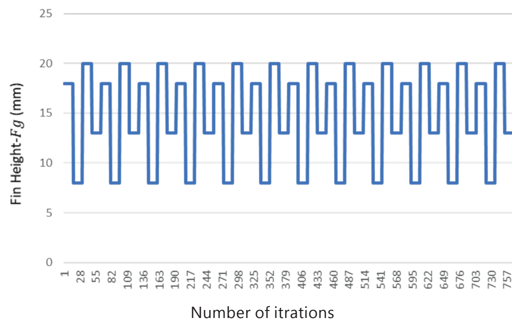

(a)

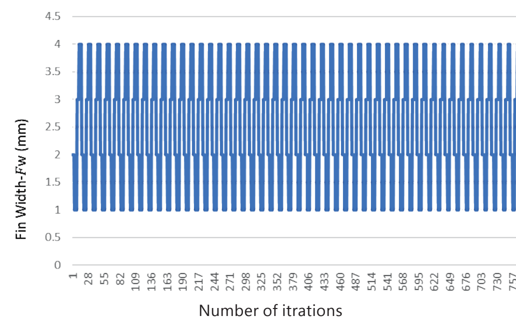

(b)

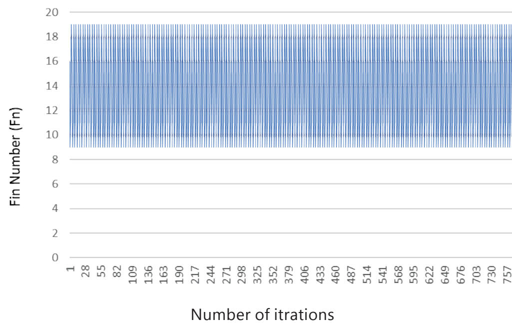

(c)

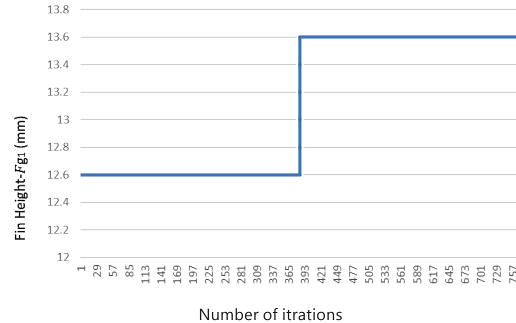

(d)

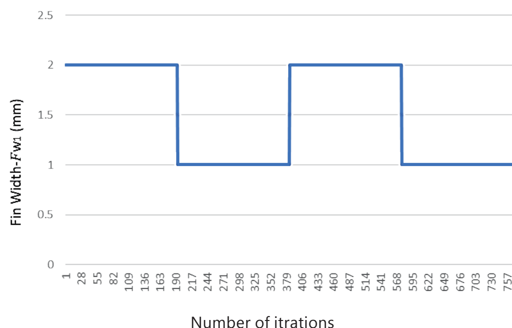

(e)

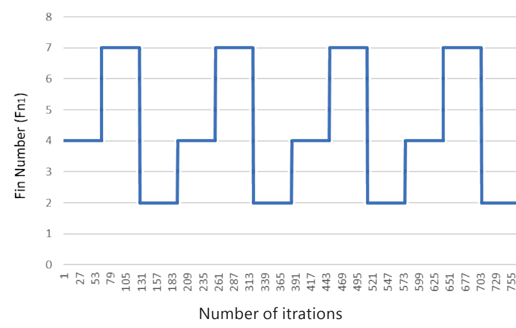

(f)

Fig. 11. (Color online) Optimization of parameters through iteration. (a) Iteration of F_g, (b) iteration of F_w, (c) iteration of F_n, (d) iteration of F_{g1}, (e) iteration of F_{w1}, and (f) iteration of F_{n1}.

3.2 Forced convection

In response to the impact of environmental climate temperature, this study not only adopts natural convection for heat dissipation in the current state but also considers the potential for high-temperature environments in the future. In such scenarios, network communication devices must employ forced convection for cooling to improve heat dissipation efficiency and system stability. Therefore, the router used in this study has two main heat-generating units: CPU and BOSA, with maximum operating temperature limits of 105 and 90 ℃, respectively. When the real-time temperature of either CPU or BOSA approaches its corresponding temperature threshold (CPU: 100 ℃; BOSA: 85 ℃), the fan will be activated to perform forced convection for effective heat dissipation. Conversely, when the temperatures of both CPU and BOSA are below their corresponding temperature thresholds, the natural convection heat dissipation mechanism will be maintained. The relevant hardware diagram for the router is shown in Fig. 12.

To address potential high-temperature environments, forced convection was introduced by adding a fan to the system. Ambient temperatures of 60, 65, and 70 ℃ were considered in the simulation. Figures 13(a) and 13(b) show CPU and BOSA temperature responses under natural convection (without a fan). BOSA showed the temperature of 90 ℃ at an ambient temperature of around 66.5 ℃, while CPU reached its limit of 105 ℃ at 72.5 ℃. In contrast, Figs 14(a) and 14(b) demonstrate that with forced convection, BOSA maintained its temperature below its limit until the temperature reached 82.5 ℃, and CPU to 89 ℃. Therefore, the fan significantly extended the safe operating range, delaying thermal failure by approximately 16 ℃ for CPU and BOSA. Figures provide empirical and numerical evidence that the sensor-driven approach is superior to traditional static cooling. The sensor integration not only enhances monitoring accuracy but also enables adaptive cooling responses, ensuring operational stability under demanding thermal conditions.

3.3 Temperature distribution

Figure 15 shows the temperature distribution of the device casing under natural and forced convection at ambient temperatures of 60, 65, and 70 ℃. Without a fan, heat accumulation led to uneven distribution and large hot spots, particularly at 70 ℃, where the BOSA reached a failure state. With forced convection, airflow removes heat more effectively, producing a more uniform temperature distribution and preventing dangerous hot zones.

3.4 Sensitivity of enclosure and heat sink parameters

To refine the thermal optimization of the network device, a sensitivity analysis was conducted on the enclosure hole design and the internal heat sink topology. This analysis was performed under a high-temperature environment with the external ambient set to 90 ℃, representing extreme operating conditions. The maximum allowable temperatures for BOSA and CPU are 90 and 105 ℃, respectively, and the thermal design aims to maintain both components below these

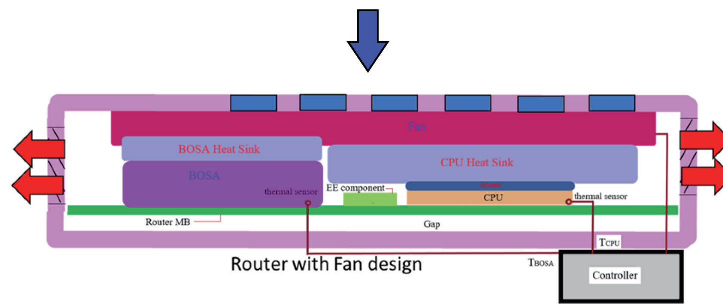

Fig. 12. (Color online) Hardware diagram for the intelligent router device.

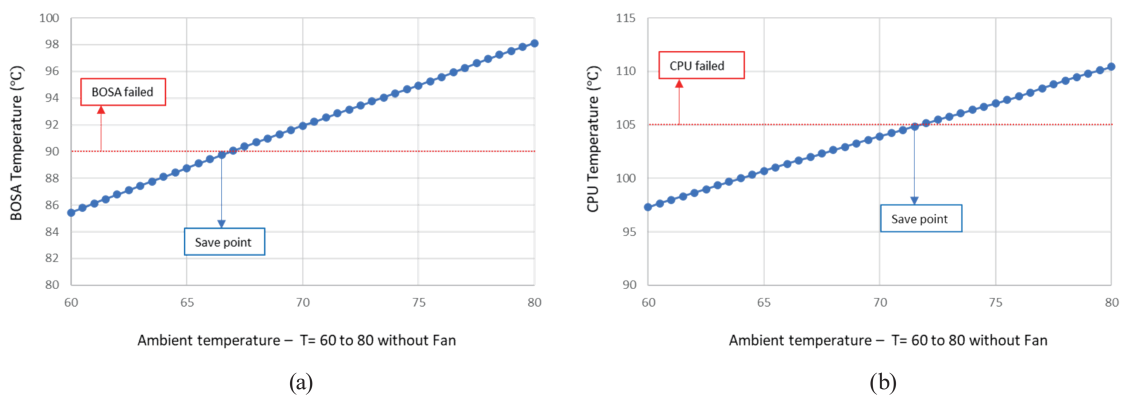

Fig. 13. (Color online) BOSA and CPU temperature limit testing simulation under fanless design with ambient temperature ranging from 60 to 80 °C (*T*: temperature in °C). (a) BOSA and (b) CPU.

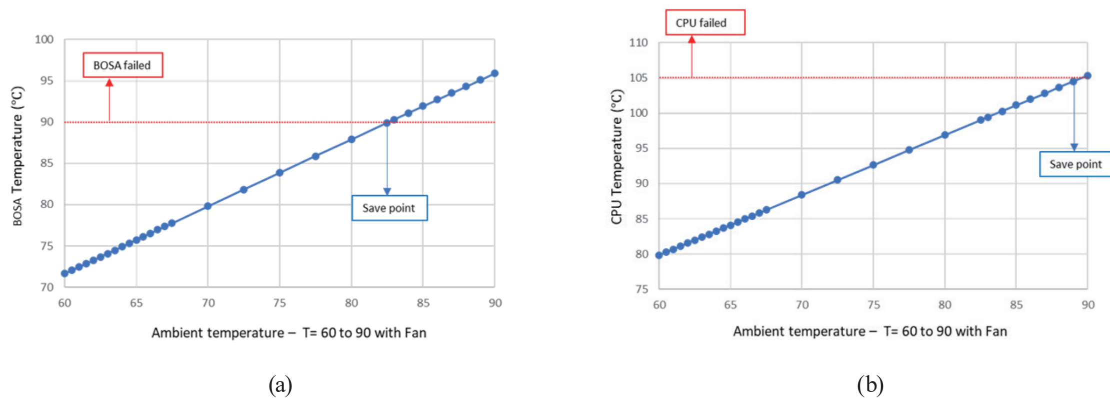

Fig. 14. (Color online) BOSA and CPU temperature limit testing simulation with fan design under ambient temperature ranging from 60 °C to 90 °C (T: temperature in °C). (a) BOSA and (b) CPU.

thresholds. Importantly, this sensitivity study was carried out under a fanless condition to isolate the effects of passive structural parameters prior to introducing forced convection.

The design includes one top hole and four surrounding holes, yielding a total of eight parameters (H_d, H_{d2}, F_h, F_w, F_n, F_{h1}, F_{w1}, and F_{n1}). Figures 16(a) and 16(b) illustrate the effects of outlet width parameters on CPU temperature. As shown in Fig. 16(a), the CPU temperature

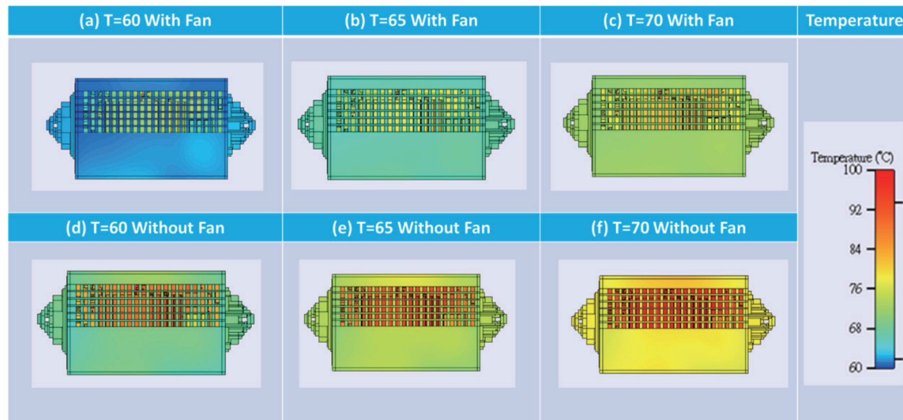

Fig. 15. (Color online) Temperature distribution simulation of the network device casing under three ambient temperatures (60, 65, and 70 °C) and two cooling mechanisms (natural and forced convection).

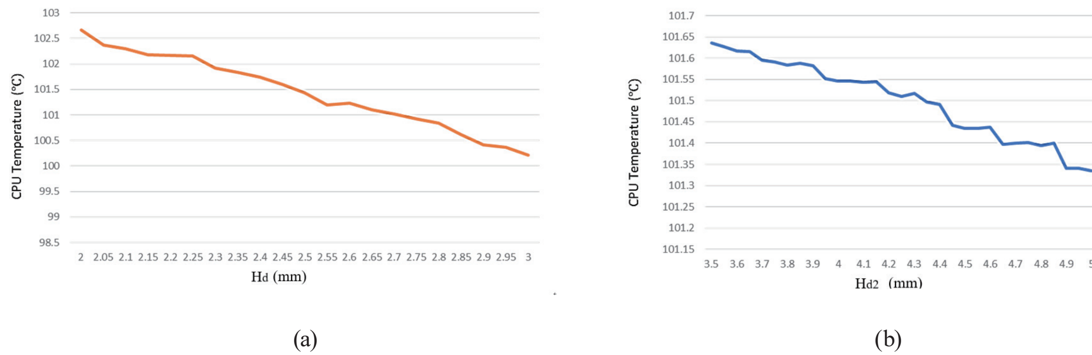

(a) (b)

Fig. 16. (Color online) Relationships of casing parameters with CPU temperature. (a) H_d and (b) H_{d2}.

decreases as the outlet width H_d increases, reaching approximately 100.2 °C when H_d = 3 mm. Similarly, Fig. 16(b) shows that increasing the upper outlet width H_{d2} to 5 mm reduces the CPU temperature to 101.33 °C. These results confirm that outlet geometry significantly affects airflow efficiency, with optimized hole dimensions contributing to improved passive cooling.

The system incorporates two heat sinks: one for CPU and one for BOSA. The CPU heat sink parameters include fin height (F_h), fin width (F_w), and the number of fins (F_n), while the BOSA heat sink parameters include F_{h1}, F_{w1}, and F_{n1}. Figures 17(a)–17(f) present the sensitivity analysis results for these variables. With 8–12 fins, the CPU temperature remained relatively stable, with optimal cooling observed at 9 or 11 fins [Fig.17(a)]. Beyond 12 fins, the CPU temperature rises sharply, indicating that excessive fin density restricts airflow. Wider fins increased the CPU temperature, with the lowest value achieved at a width of 1 mm. Narrower fins provide superior heat dissipation [Fig. 17(b)]. Taller CPU fins reduced the CPU temperature, with significant improvement up to 20 mm. Beyond this height, the benefit plateaus, with an optimal CPU temperature of 101 °C [Fig. 17(c)].

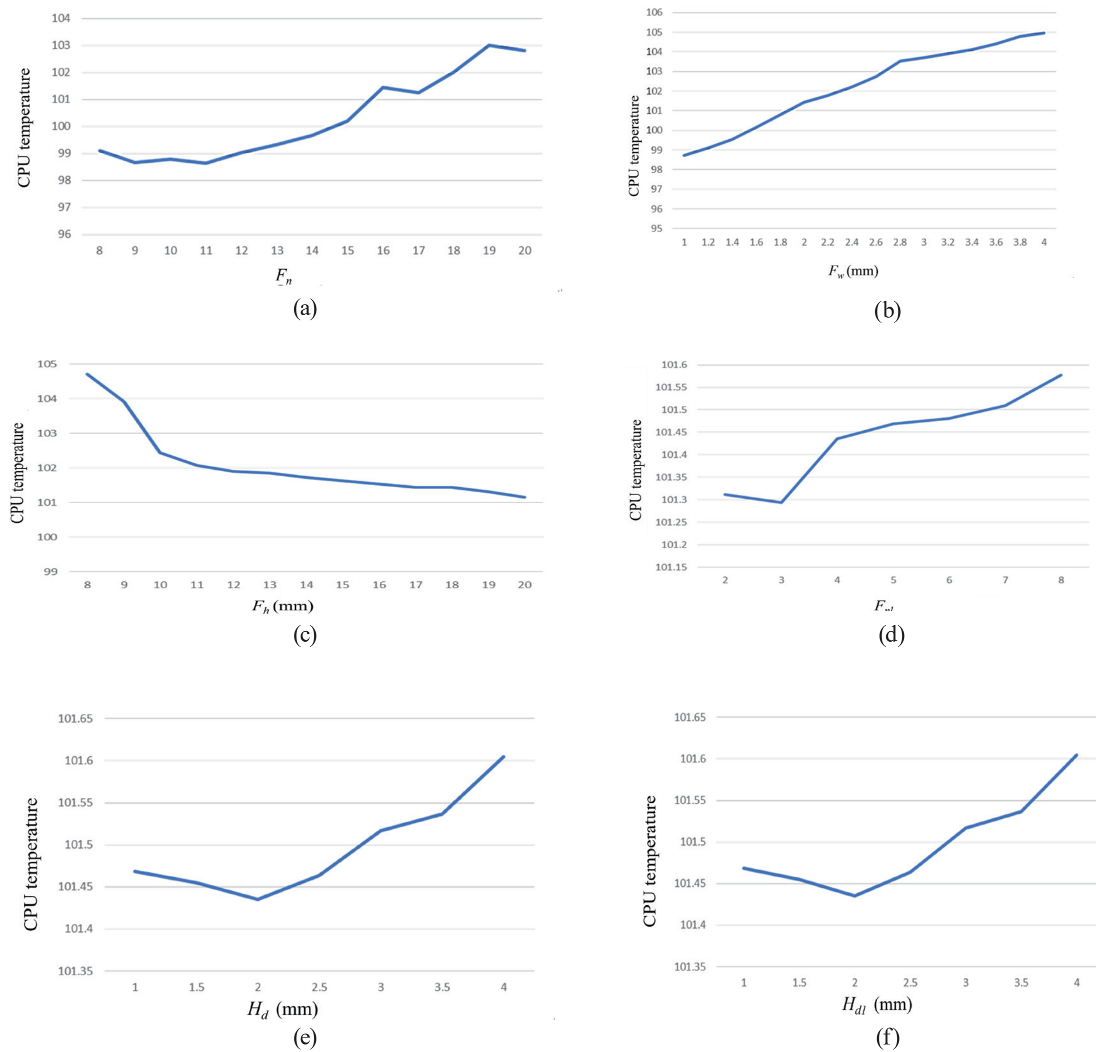

Fig. 17. (Color online) Relationships of internal heat sink parameters with CPU temperature. (a) F_n, (b) F_w, (c) F_h, (d) F_{n1}, (e) H_d, and (f) H_{d1}.

The impact of the BOSA cooling fin number on the system's thermal state is shown in Fig. 17(d), where increasing the number of fins increased the CPU temperature. Optimal cooling performance was achieved with only 2 to 3 fins, as this configuration provides the most effective balance between internal airflow and heat dissipation efficiency. Regarding the BOSA fin width [Fig. 17(e)], the CPU temperature reached its minimum when the fin width was 2 mm. This finding suggests that a 2 mm dimension achieves the ideal geometric trade-off for maximizing cooling effectiveness within the device enclosure. The BOSA fin height showed no significant correlation with the CPU temperature within a range of 11.2 to 13.6 mm [Fig. 17(f)]. This lack of a significant trend indicates that variations in BOSA fin height have a limited effect on the CPU's thermal management, allowing the sensor-driven control system to focus on more critical parameters for temperature regulation.

The sensitivity analysis results demonstrate that passive design parameters, including fin geometry and enclosure hole dimensions, play an important role in thermal regulation. However, even with optimized passive configurations, CPU and BOSA temperatures approached their operational limits under extreme conditions. This underscores the necessity of the integrated sensor-driven control system. By leveraging real-time sensor feedback, the device can dynamically compensate for the limitations of passive cooling, activating the fan at the 65 ℃ threshold to ensure safe operation and extend thermal reliability.

4. Discussion

The sensitivity analysis results (Figs. 16 and 17) demonstrate that enclosure hole sizes and fin geometries are critical determinants of the system's thermal equilibrium. As shown in Figs. 16(a) and 16(b), the optimization of the exhaust vent dimensions (H_d and H_{d1}) affects the air volume and exhaust velocity. By precisely tuning the outlet width to 3 mm and the upper outlet to 5 mm, the CPU temperature was reduced significantly, confirming that geometric venting parameters dictate the baseline efficiency of natural convection.

The detailed analysis of the BOSA heat sink topology [Figs. 17(d) and 17(f)] reveals a complex relationship between fin geometry and cooling performance. The BOSA module showed an inverse correlation between fin density and cooling efficiency; increasing the number of fins beyond 3 increased the CPU temperature. This suggests that in compact, fanless enclosures, an excessive number of fins can impede internal airflow, creating stagnant heat zones. Similarly, a fin width of approximately 2 mm was found to be the optimal threshold for balancing thermal mass with airflow clearance. The relative stagnation of CPU temperature regardless of BOSA fin height (11.2–13.6 mm) indicates that once a minimum surface area is achieved, vertical extension provides diminishing returns for secondary component cooling.

These findings guided the engineering optimization process, which identified the ideal parameters for the CPU and BOSA heat sinks. Under natural convection, the optimized configurations reduced the CPU temperature to 93 under a 60 ℃ ambient condition. However, a limitation was observed. Without forced convection, the system reached its thermal threshold when the ambient temperature exceeded 66.5 ℃ for the BOSA and 72.5 ℃ for the CPU. The subsequent integration of a fan extended the safe operating range significantly to 82.5 ℃ for BOSA and 88 ℃ for CPU. This indicates the necessity of a hybrid cooling strategy.

The results underscore the transformative role of temperature sensors in transitioning from static to intelligent thermal management. Sensors function as the nervous system of the device by providing high-fidelity, real-time data to the controller. They activate the fan only when specific thresholds of temperature occur. This sensor-guided regulation ensures that the cooling response is dynamic, adjusting to both fluctuating workloads and rising ambient temperatures, such as those predicted by global warming trends. By combining CFD-based structural optimization with sensor-driven active control, this research demonstrates a robust framework for next-generation electronics, where compact geometries and high power densities demand adaptive, data-informed cooling solutions.

The primary challenge addressed in this study is that existing thermal management designs predominantly rely on simple on/off fan control strategies. Although such approaches can satisfy

basic cooling requirements, they often lead to suboptimal trade-offs between acoustic noise and cooling efficiency under varying thermal load conditions, thereby adversely affecting user experience. In the present work, a fundamental framework is proposed in which temperature sensor feedback is used to regulate fan activation, ensuring that the system operates stably within a safe temperature range. Future research may further advance this approach by developing optimal fan cooling strategies that dynamically adjust fan speed in response to real-time temperature variations. In addition, considering the impact of fan noise on user comfort, subsequent studies should integrate fan noise modeling with thermal performance simulations to achieve a balanced design that simultaneously satisfies acoustic requirements and cooling efficiency.

5. Conclusion

The thermal optimization of network communication devices was explored by conducting a sensitivity analysis on eight parameters related to heat dissipation structures, fin topology, and enclosure perforation design for CPU and BOSA. The vent design was fixed before optimizing the remaining parameters, and numerical simulation results at an ambient temperature of 25 °C and experimental results confirmed the accuracy of the CFD model, which achieved a simulated CPU temperature of 102.5 °C compared with the measured 101.8 °C, yielding only a 0.7% error. The results demonstrated that perforation geometry exerts a strong affect on CPU temperature. Through 756 design iterations, the optimal CPU heat sink configuration (F_h = 20 mm, F_w = 1 mm, and F_n = 9) reduced the CPU temperature to 93 °C, while sensitivity analysis revealed that narrower fins and moderate fin counts provided superior cooling efficiency, whereas excessive fin density restricted airflow and increased thermal resistance. We compared natural and forced convection under varying ambient conditions, showing that forced convection significantly extended the safe operating range from 66.5 to 82.5 °C for BOSA and from 72.5 C to 88 °C for CPU.

The focus of this study is not merely to propose an intuitive thermal dissipation criterion, but to investigate the coupling relationships among thermal design, airflow rate, and system heat load in practical products. Furthermore, a microcontroller-based temperature control system is integrated to intelligently regulate fan activation, thereby achieving optimal thermal management for the router system. Although it may be intuitively understood that a hybrid cooling strategy is required, this study further validates through systematic simulations and design analyses that a single cooling strategy may be insufficient under more demanding operating conditions, such as near-military or high-reliability applications. Therefore, the contribution of this work lies in providing an evaluation methodology applicable at the product design stage, enabling thermal design, airflow, and system heat load to be assessed not solely based on empirical judgment, but through more reliable numerical temperature predictions. Combined with an intelligent fan control system, this approach mitigates overheating effects of high ambient temperatures and reduces the risk of thermal failure. By integrating natural convection with sensor-triggered forced convection, the device regulates cooling in response to real-time thermal data. Embedded sensors act as the device's nervous system, continuously monitoring component temperatures and activating the fan only when thresholds are approached, thereby ensuring stability while

conserving energy. The results also showed that advancing sensor technology is required to transform passive thermal monitoring to an active, intelligent one. By leveraging real-time feedback to adapt cooling behavior, the device compensates for the limitations of passive designs and enhances the reliability and longevity of semiconductor materials in compact enclosures. This sensor-driven approach enables a scalable framework for managing complex thermal profiles in next-generation portable electronics, where miniaturization and high power densities demand adaptive, data-informed cooling solutions.

References

1 H. Attar, H. Issa, J. Ababneh, M. Abbasi, A. A. A. S. M. Khosravi, and R. S. Agieb: Comput. Intell. and Neurosci. **2022** (2022) 2476841. https://doi.org/10.1155/2022/2476841.
2 G. Ancans, A. Stafecka, V. Bobrov, A. Ancans, and J. Caiko: Latv. J. Phys. Tech. Sci. **54** (2017) 69. https://doi.org/10.1515/lpts-2017-0028
3 Z. Li, H. Luo, Y. Jiang, H. Liu, L. Xu, K. Cao, H. Wu, P. Gao, and H. Liu: Appl. Therm. Eng. **251** (2024) 123612. https://www.sciencedirect.com/science/article/abs/pii/S1359431124012808
4 Q. L. Xiong, T. Shimada, and T. Kitamura: J. Appl. Phys. **133** (2023) 185902. https://doi.org/10.1063/5.0144016
5 Q. Wang, Y. Wu, S. Niu, and X. Zhao: Energies **15** (2022) 3249. https://doi.org/10.3390/en15093249
6 H. Nakano, K. Watari, H. Hayashi, and K. Urabe: J. Am. Ceram. Soc. **85** (2004) 3093. https://doi.org/10.1111/j.1151-2916.2002.tb00587.x
7 C. Giorgi and F. Zullo: Energies **14** (2021) 1643. https://doi.org/10.3390/en14061643
8 ASHRAE Technical Committee: https://www.scribd.com/document/656530216/ASHRAE-Datacom-Series-ASHRAE-Technical-Committee-Thermal-Guidelines-for-Data-Processing-Environments-ASHRAE-2021 (accessed March 2026).
9 E. Pop, E. Sinha, and K. E. Goodson: Proc. IEEE **94** (2006) 1587. https://doi.org/10.1109/JPROC.2006.879794
10 Z. He, Y. Yan, and Z. Zhang: Energy **216** (2021) 119223. https://doi.org/10.1016/j.energy.2020.119223
11 W. He, J. Zhang, R. Guo, C. Pei, H. Li, S. Liu, J. Wei, and Y. Wang: Appl. Energy **327** (2022) 120048. https://doi.org/10.1016/j.apenergy.2022.120048.
12 B. Li, J. C. E. Yong, L. J. Yu, Z. Zhang, X. Yang, and C. Peng: E3S Web of Conf. **439** (2023) 01007. https://doi.org/10.1051/e3sconf/202343901007
13 Y. Yuan, J. Shim, S. Lee, D. Song, and J. Kim: Sustainability **12** (2020) 8974. http://dx.doi.org/10.3390/su12218974
14 L. Sisk and D. Allen: Proc. 2014 36th Int. Telecommunications Energy Conf. (INTELEC, 2014) 1. https://doi.org/10.1109/INTLEC.2014.6972161.
15 Y. L. Chen, M. F. Chang, C. W. Yu, X. Z. Chen, and W. Y. Liang: Sensors **18** (2018) 3068. https://doi.org/10.3390/s18093068
16 A. Das, G. V. Merret, M. Tribastone, and B. M. Al-Hashim: IEEE Trans. Comput.-Aided Des. Integr. Circuits Syst. **35** (2015) 1358. https://doi.org/10.1109/TCAD.2015.2504875
17 D. W. Yoo and Y. K. Joshi: IEEE Trans. Device Mater. Rel. **4** (2005) 641. https://doi.org/10.1109/TDMR.2004.840854
18 K. C. Chen, M. C. Chiu, Y. H. Wang, S. M. Cho, and T. S. Lan: Sens. Mater. **37** (2025) 1681. https://doi.org/10.18494/SAM5463